Complete characterization of single-cycle double ionization of argon from the nonsequential to the sequential ionization regime

M. Kübel,[1,*] C. Burger,[1,2] Nora G. Kling,[1,3] T. Pischke,[1] L. Beaufore,[1] I. Ben-Itzhak,[3] G. G. Paulus,[4,5] J. Ullrich,[6,7] T. Pfeifer,[6] R. Moshammer,[6] M. F. Kling,[1,2] and B. Bergues[2,†]

[1]*Department für Physik, Ludwig-Maximilians-Universität, D-85748 Garching, Germany*

[2]*Max-Planck-Institut für Quantenoptik, D-85748 Garching, Germany*

[3]*J. R. Macdonald Laboratory, Department of Physics, Kansas State University, Manhattan, Kansas 66506, USA*

[4]*Institut für Optik und Quantenelektronik, Friedrich-Schiller-Universität, D-07743 Jena, Germany*

[5]*Helmholtz Institut Jena, D-07743 Jena, Germany*

[6]*Max-Planck-Institut für Kernphysik, D-69117 Heidelberg, Germany*

[7]*Physikalisch-Technische Bundesanstalt, D-38116 Braunschweig, Germany*

(Received 12 February 2016; published 23 May 2016)

Selected features of nonsequential double ionization have been qualitatively reproduced by a multitude of different (quantum and classical) approaches. In general, however, the typical uncertainty of laser pulse parameters and the restricted number of observables measured in individual experiments leave room for adjusting theoretical results to match the experimental data. While this has been hampering the assessment of different theoretical approaches leading to conflicting interpretations, comprehensive experimental data that would allow such an ultimate and quantitative assessment have been missing so far. To remedy this situation we have performed a kinematically complete measurement of single-cycle multiple ionization of argon over a one order of magnitude range of intensity. The momenta of electrons and ions resulting from the ionization of the target gas are measured in coincidence, while each ionization event is tagged with the carrier-envelope phase and intensity of the 4-fs laser pulse driving the process. The acquired highly differential experimental data provide a benchmark for a rigorous test of the many competing theoretical models used to describe nonsequential double ionization.

DOI: 10.1103/PhysRevA.93.053422

I. INTRODUCTION

Strong-field multiple ionization of atoms is widely regarded as a classic example of multielectron dynamics in an external field and has attracted considerable interest of experimentalists [1–6] and theorists [7–11] alike. Double ionization in particular is a process characterized by different intensity-dependent regimes [12]. At high laser intensities, close to the saturation intensity for single ionization, double ionization is dominated by sequential double ionization (SDI), which can be described within the single-active-electron approximation. At lower intensity, nonsequential double ionization (NSDI) sets in, a regime where the double-ionization probability is orders of magnitude higher than predicted by SDI [2,12]. Different models incorporating electron correlation have thus been proposed to describe the dynamics leading to NSDI, as described in a recent review [13].

Detailed information about the NSDI dynamics has been obtained with the development of kinematically complete experiments, in which the momenta of electrons and ions generated in the ionization process are measured in coincidence [14,15]. The results from these experiments [4,16–19] indicate that the ionization of the second electron in NSDI is triggered by the recollision of the first ionized electron with the parent ion [20]. In conventional experiments using multicycle laser pulses, however, multiple recollisions of the first electron with the parent core may significantly complicate the NSDI dynamics [21,22], impeding quantitative comparison of experiment and theory. Confining NSDI to a single laser cycle using carrier-envelope phase (CEP)-tagged few- [23] and near-single-cycle [24,25] pulses has recently allowed the suppression of multiple recollisions, thus transposing the ideal conditions assumed in many models into the laboratory (see Ref. [26] for a recent review on single-cycle NSDI). It was demonstrated indeed that single-cycle and multicycle NSDI dynamics of argon are dramatically different, with a marked transition occurring in the few-cycle regime [22,27,28].

The cross-shaped two-electron momentum spectrum (TEMS) observed in single-cycle NSDI [24] indicates asymmetric energy sharing between the two electrons and can be well understood assuming recollisional excitation with subsequent ionization by the laser field [8,29]. The exact underlying physics, however, gave rise to some debate. While semiclassical models ascribe the asymmetric energy sharing to a depletion effect [24], quantum mechanical calculations are able to generate the cross-shaped TEMS without resorting to depletion, indicating that it is rather the symmetry of the excited state that is playing a key role [28,30].

This debate shows that the ultimate assessment of theoretical models requires a systematic and fully differential experimental study of single-cycle NSDI over a broad range of intensities. Although highly desirable, such kinematically complete NSDI data have only been recorded for a few intensity values in independent experiments. Because of the generally low accuracy of the absolute intensity determination, the set of available data does not strongly constrain theoretical models as the intensity value can be adjusted independently for each measurement.

Here we remedy this problem with a comprehensive study of multiple ionization of argon in the single-cycle regime,

*Matthias.kuebel@physik.uni-muenchen.de

†boris.bergues@mpq.mpg.de

in which we resolve the evolution of the CEP-dependent two-electron dynamics along the intensity-dependent double-ionization yield curve. Taking advantage of the CEP-dependent observables, we perform a characterization of the transition from the nonsequential to the sequential regime that sets a benchmark for the theoretical description of NSDI. The constraints imposed by our measurements are demonstrated by a rigorous comparison of the experimental data to predictions from a semiclassical model, which adequately described the results at a single intensity value [24].

II. EXPERIMENTAL SETUP

In our experiment, intense 4-fs [full width at half maximum (FWHM) in intensity] laser pulses with a center wavelength of 750 nm are generated at a repetition rate of 10 kHz using a Femtolasers Femtopower HR CEP4 chirped-pulse amplification (CPA) based laser system. The CEP of the laser is stabilized using the feed-forward technique [31], controlled by varying the dispersion in the CPA stage, and measured using an f-2f interferometer. The laser pulse energy is adjusted with a motorized neutral density filter wheel and the beam is sent into a reaction microscope (REMI) [15]. The laser power is measured with a fast power meter at the exit of the REMI. In the REMI, the laser pulses are focused into a cold-gas jet of argon atoms. In order to keep the count rate close to 0.1 ions per laser shot when changing the intensity, the extension of the gas target along the laser propagation direction is controlled using a slit of variable width to cut into the gas stream. The momenta of ions and electrons are recorded in coincidence using a pair of time- and position-sensitive detectors. The data recorded with the REMI are correlated with the simultaneously measured CEP and average power of the laser pulses. The focal laser intensity is estimated from the measured power dependence of the $10U_P$ cutoff in the single-ionization photoelectron spectra of Ar.

III. RESULTS AND DISCUSSION

In order to study the multiple-ionization processes over a large intensity range, the data in the high- and low-intensity regions were acquired in two separate measurements using focusing mirrors with focal lengths of $f = 10$ and 17.5 cm, respectively. The intensity ranges of the two measurements overlap between 1.4 and 2.4×10^{14} W cm^{-2}, which allows for a quantitative comparison of the two data sets. The effect of the different focusing geometries on the intensity distribution in the focal volume is addressed in Appendix E. It is shown there that the discrepancies between the two data sets in the overlap region are imputable to the slightly different focal volume averaging conditions in the two measurements. Despite these discrepancies, the intensity dependence of the measured observables exhibits the same qualitative behavior for both data sets.

The measured ratio of double- to single-ionization yields is shown in Fig. 1 together with the corresponding CEP-averaged TEMS. The yield ratio exhibits the characteristic knee shape [2,12] with an inflexion point around 3×10^{14} W cm^{-2} and approaches the magnitude expected from pure SDI near 6×10^{14} W cm^{-2}. The evolution of the curve with increasing intensity is accompanied by significant changes in the TEMS.

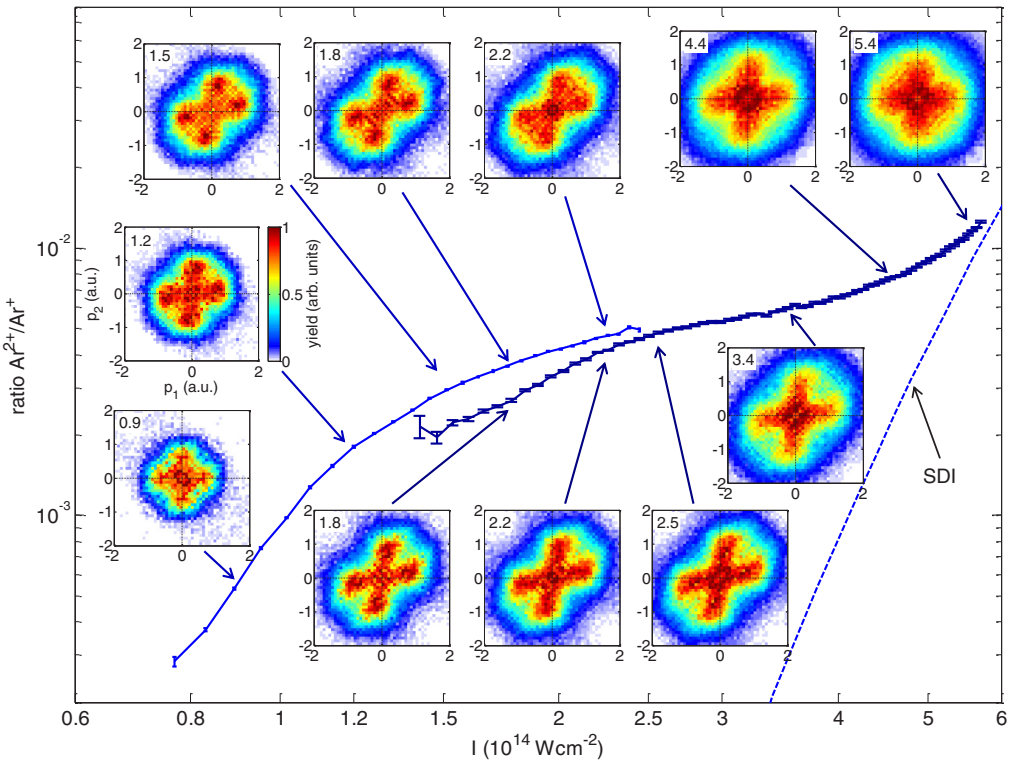

FIG. 1. Ratio of the recorded yields of Ar^{2+} and Ar^{+} ions plotted as a function of intensity for both data sets (light and dark blue, respectively). The measured TEMS are CEP averaged and contain events collected in a ±5% intensity interval around the value indicated in units of 10^{14} W cm^{-2} in each panel. The dashed blue line is the calculated intensity-dependent yield ratio expected from SDI.

In the TEMS the double-ionization yield is plotted as a function of the momenta p_1 and p_2 of the first and second electrons along the polarization direction, using momentum bins of 0.08 a.u. Since the two electrons are not distinguishable, the distributions are symmetrized with respect to the main diagonal. Each plot is generated following the procedure detailed in Ref. [22] and contains between 10 500 and 160 000 events collected over an intensity range of ±5% of the indicated intensity value.

At low intensity (0.9×10^{14} W cm^{-2}) the distribution assumes a cross shape with maximum signal around $(p_1, p_2) = 0$. At higher intensity [$(1.2–1.9) \times 10^{14}$ W cm^{-2}] the arms of the cross become slightly tilted towards the main diagonal while maxima build up at their extremities that extend to higher momenta. At even higher intensity [$(2.2–2.5) \times 10^{14}$ W cm^{-2}] a maximum appears again at the center. This low-momentum signal at the center becomes even broader when the intensity is further increased [$(3.4–4.4) \times 10^{14}$ W cm^{-2}] and dominates the whole distribution at the highest intensity used in the experiment (5.4×10^{14} W cm^{-2}).

In order to demonstrate the stringent constraints that the measurements impose on the theoretical description of strong-field double ionization, we compare the experimental results with a semiclassical model for SI, SDI, and NSDI. For NSDI the recollisional excitation with a subcycle depletion (RESD) mechanism [24] is used. The calculation and fitting procedure is described in detail in Appendices A and B. Best agreement between measured and calculated TEMs is obtained if a scaled intensity I_{th}, which is 2.5 higher than the measured intensity I, is used in the calculations.

For this intensity I_{th}, the NSDI calculations shown in Fig. 2(a) qualitatively reproduce the intensity dependence of the TEMS in the lower-intensity range (up to a measured intensity $I = 2.2 \times 10^{14}$ W cm^{-2}). As in the experimental data, the signal of the TEMS at low intensities is concentrated at small momentum values, while local maxima emerge on the arms of the cross shape at higher intensities. In the simulations this behavior results from the depletion of the excited-state population [24]. At low intensity, where depletion is negligible, the second electron is emitted near a cycle maximum and therefore does not acquire substantial momentum. When the intensity is increased, depletion shifts the second electron emission to an earlier time before the cycle maximum, which results in a larger momentum transfer and an elongation of the cross-shaped TEMS.

For intensities beyond $I = 2.2 \times 10^{14}$ W cm^{-2} (i.e., $I_{\text{th}} = 5.4 \times 10^{14}$ W cm^{-2}), the NSDI model fails to reproduce the yield at the origin of the TEMS and breaks down. The SDI calculations, presented in Fig. 2(b), show that the expected onset of SDI provides a consistent explanation for the low-momentum contribution to the signal at higher intensities. Since in SDI the electrons preferentially tunnel out at the peak of the laser field, there is no significant momentum transfer to the electron and the signal concentrates at the origin of the TEMS. Despite the qualitative agreement between calculated and measured spectra, the overestimation of the measured intensity by a factor 2.5 is incompatible with the 20% uncertainty in the experimental intensity determination. We attribute this discrepancy to the systematic underestimation of electron momenta by semiclassical approaches [32].

In Fig. 3 the measured intensity-dependent ratio of double- to single-ionization yields (markers) is compared to the sum (dotted lines) of the calculated SDI (dashed lines) and NSDI (solid lines) contributions. When the yield ratio is calculated using the measured intensity (blue lines) qualitative agreement is obtained, assuming an impact excitation probability of 1%. When the same calculation is performed with the scaled intensity I_{th}, which yields a reasonable description of the momentum distributions, the calculated yield ratio (green lines) does not agree with the measured one.

In order to investigate the intensity dependence of CEP effects for single and double ionization, the asymmetry

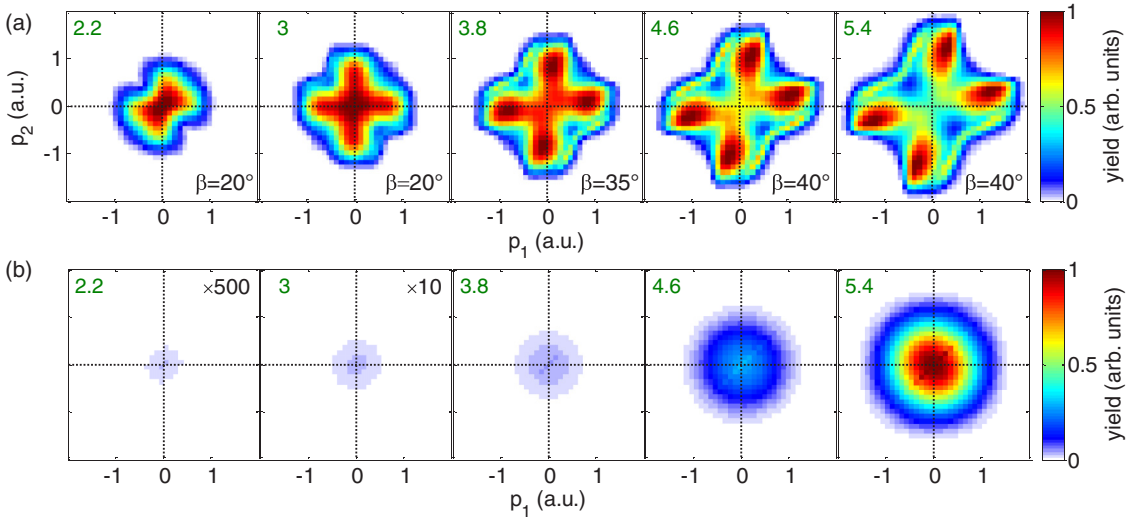

FIG. 2. Calculated CEP-averaged TEMS for double ionization of Ar assuming (a) the RESD model for NSDI and (b) SDI. The number in the top left corner of each TEMS indicates the scaled intensity I_{th}, in units of 10^{14} W cm^{-2}, used in the calculation. The TEMS in (a) are normalized to their respective maxima, while the spectra in (b) are normalized to the maximum signal at the highest intensity shown. For visibility, the SDI signal calculated for the two lowest intensity values is enhanced by a factor of 500 or 10, respectively. The value of β, the only free parameter of the RESD model (see Appendix A), is indicated in each panel.

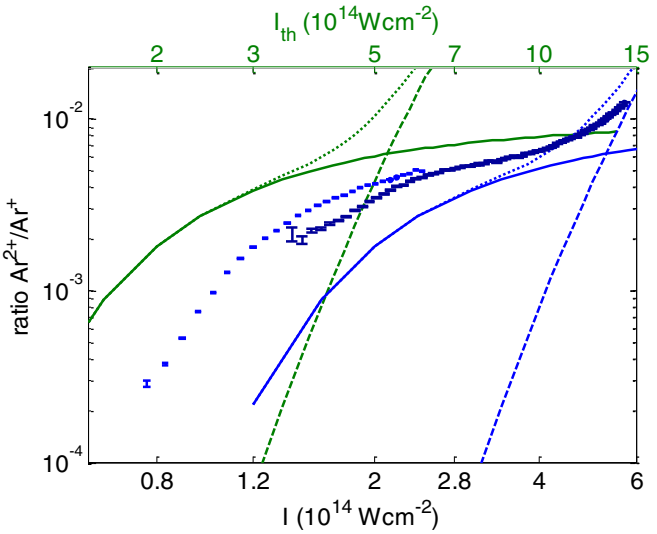

FIG. 3. Comparison of the measured intensity-dependent ratio of double to single ionization yields (markers) to the calculation results (lines). The dashed and solid lines represent the calculated SDI and NSDI contribution, respectively. The sum of these contributions is plotted as a dotted line. The set of blue curves on the right and the set of green curves on the left have been calculated using the measured I and scaled intensities $I_{\rm th}$, respectively.

parameter

$$A(I,\phi) = \frac{N_+(I,\phi) - N_-(I,\phi)}{N_+(I,\phi) + N_-(I,\phi)} \tag{1}$$

is evaluated as a function of intensity I and CEP ϕ. Here $N_+(I,\phi)$ $[N_-(I,\phi)]$ denotes the yield of ions with positive (negative) momentum along the laser polarization. For each intensity, $A(I,\phi)$ is fitted with the sinusoidal function

$$A(I,\phi) = A_0(I)\sin[\phi + \phi_0(I)]. \tag{2}$$

The obtained asymmetry amplitudes $A_0(I)$ and phases $\phi_0(I)$ are plotted in Figs. 4(a) and 4(b), respectively, and compared to predictions of the SI, NSDI, and SDI models.

The measured Ar^+ and Ar^{2+} asymmetry amplitudes shown in Fig. 4(a) decay with increasing intensity. This is due to the increasing number of laser half cycles contributing to ionization with increasing intensity. While this trend is qualitatively reproduced by the SI and NSDI calculations in a small range of measured intensities I between 1.5 and 2.5×10^{14} W cm^{-2}, the model fails to give a proper description of the measurement over the whole intensity range.

A similar conclusion holds for the phase of the Ar^+ and Ar^{2+} asymmetry parameter plotted in Fig. 4(b). When the intensity is increased, the phase difference between the Ar^+ and Ar^{2+} asymmetries monotonically decreases from $3/2\pi$ to $3/4\pi$. The slopes of the intensity-dependent phases for single and double ionization have opposite sign up to an intensity $I \approx 3.5 \times 10^{14}$ W cm^{-2}, where the Ar^{2+} curve flattens. Here again the SI and NSDI calculations are qualitatively consistent with the measurements for $I < 2 \times 10^{14}$ W cm^{-2}. For higher intensities, however, the results of calculations and measurement are inconsistent. We show in Appendix D that, as in the case of the intensity-dependent yield ratio, much better overall agreement between calculation and measurement is obtained

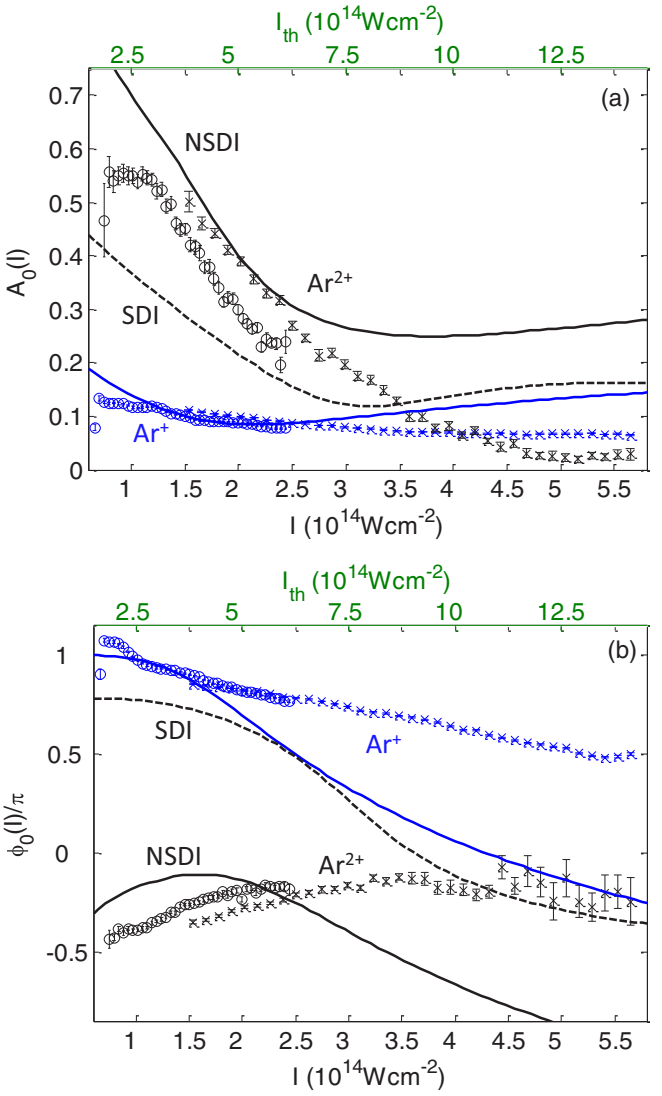

FIG. 4. Intensity dependence of the CEP-dependent asymmetries in the Ar^+ and Ar^{2+} ion yields, encoded as blue and black, respectively. The CEP-dependent asymmetry is parametrized according to Eq. (2) and the intensity dependences of $A_0(I)$ and $\phi_0(I)$ are shown in (a) and (b), respectively. The data recorded in the low-intensity and high-intensity measurements are represented by circles and crosses, respectively. The blue solid line corresponds to the SI calculations. The solid and dashed black lines display the predictions by the semiclassical NSDI and SDI models, respectively. Here the unknown phase offset is chosen such that the values of $\phi_0(I)$ recorded for Ar^+ at $I_{\rm th} = 3 \times 10^{14}$ W cm^{-2} agree with the result of the SI calculation.

for the Ar^+ and Ar^{2+} phases and the Ar^+ asymmetry amplitude when the measured intensity is used in the calculation. In this case, however, no agreement is obtained for the Ar^{2+} asymmetry amplitude and none of the momentum spectra are nearly correctly reproduced.

IV. CONCLUSION

In summary, we have performed a kinematically complete measurement of multiple ionization of argon in the single-cycle limit, resolving the process in the CEP over a wide range of intensities. While single observables, taken separately,

can be fitted rather accurately by a semiclassical model, consideration of the entire coherent set of measured quantities precludes a consistent description of the experimental observations by the same model. On the one hand, these results demonstrate that a good fit of individual observables, which is commonly used for the assessment of NSDI models, has only limited significance. On the other hand, the results show that because of their much stronger constraints, our highly differential data will challenge existing models, finally enabling their quantitative assessment and paving the way for future theoretical developments.

ACKNOWLEDGMENTS

We thank Ferenc Krausz for his support and for making specialized equipment available to us. B.B. acknowledges additional support from Laszlo Veisz. We are grateful for support from the Max Planck Society via the IMPRS-APS, the DFG via LMUexcellent, the Cluster of Excellence: Munich Center for Advanced Photonics, and the European Union via the European Research Council (ERC) Grant ATTOCO (No. 300372). I.B.-I. and N.G.K. acknowledge support from the Chemical Sciences, Geosciences, and Biosciences Division, Office of Basic Energy Sciences, Office of Science, U.S. Department of Energy, European Union under the Seventh Framework Program. L.B. is grateful for support from the DAAD through the RISE program. We also thank Hartmut Schröder and Carla Figueira de Morisson Faria for stimulating discussions.

APPENDIX A: DESCRIPTION OF THE SIMULATIONS

In the calculations of single and double ionization, the atom is located at the origin $x = 0$ of the one-dimensional coordinate system. The electric field of the laser pulse is modeled as $E(t) = E_0 \cos^2(t/\tau)\cos(\omega t + \phi)$, where E_0 is the field amplitude, ω the carrier frequency, τ the pulse duration, and ϕ the CEP. For single ionization (SI) and sequential double ionization the time-dependent population $N_{0,1,2}(t)$ of the respective Ar, Ar^+, and Ar^{2+} ground states is calculated by solving the rate equations

$$\begin{aligned} N_0(t+dt) &= N_0(t) - w_{01}N_0(t)dt, \\ N_1(t+dt) &= N_1(t) + w_{01}N_0(t)dt - w_{12}N_1(t)dt, \\ N_2(t+dt) &= N_2(t) + w_{12}N_1(t)dt, \\ N_{1,2}(t_i) &= 0, \quad N_0(t_i) = 1, \end{aligned}$$

where $t_i = -\pi/2\tau$ and w_{ij} are the parametrized ionization rates proposed by Tong and Lin [33],

$$w_{ij} = w_{\mathrm{ADK}} \exp\left(-\alpha \frac{Z_c^2 E(t)}{I_p (2I_p)^{3/2}} \right). \tag{A1}$$

Here w_{ADK} is the instantaneous Ammosov-Delone-Krainov rate [34] summed over all occupied degenerate states of the outer shell, Z_c is the charge of the parent core, I_p is the ionization potential, and α is a numerical factor adjusted such that the rate $w(t)$ fits the numerical solution of the Schrödinger equation. The value of the parameter α is 9 for Ar and 8 for Ar^+ [33].

An electron ionized at the instant t_0 enters the continuum with zero initial momentum at the tunnel exit x_t, from where it is propagated classically under the sole influence of the laser electric field. In the NSDI model, an electron that revisits the position $x = 0$ of the parent ion at a later time t_1 and carries sufficient kinetic energy E_r instantaneously excites the ion to its lowest excited state Ar^+ $(3s3p6)\,^2S_{1/2}$ with a probability $w_{01}N_0(t_0)dt$. This state has an excitation

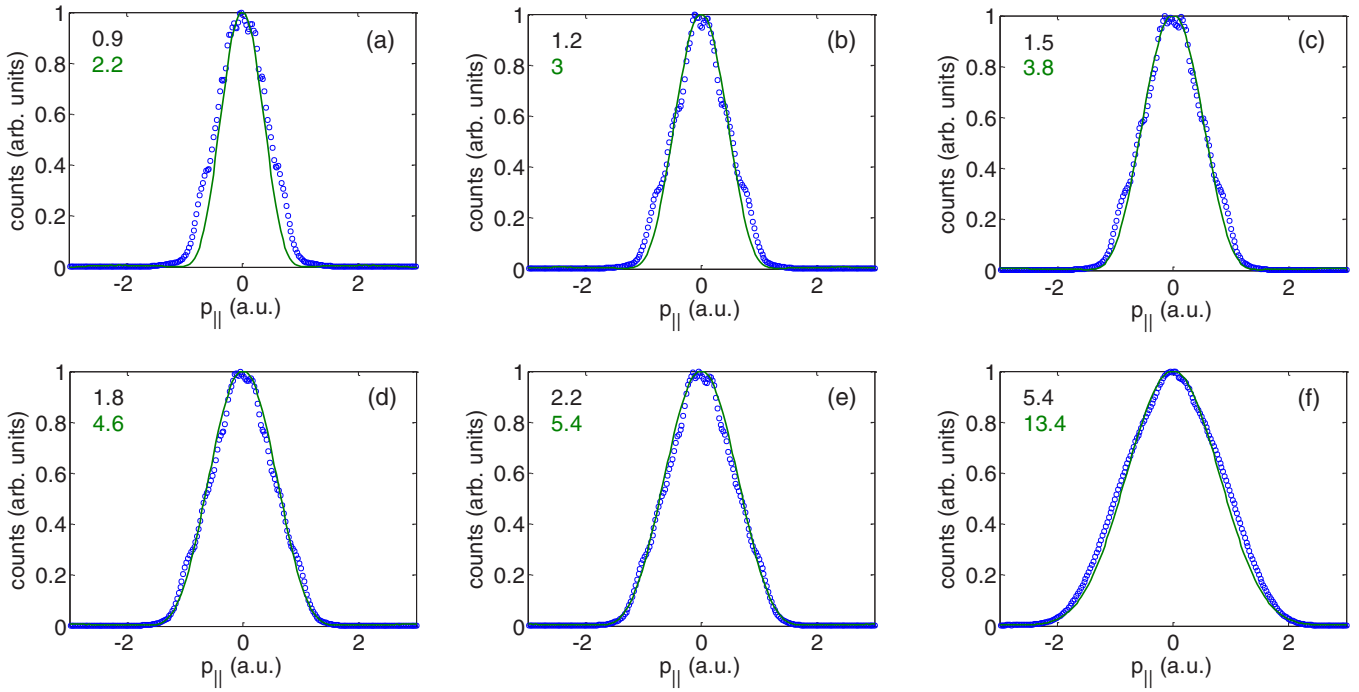

FIG. 5. (a)–(f) CEP-averged Ar^+ momentum spectra along the laser polarization (blue symbols) measured at various intensities, shown together with the simulated spectra (solid green lines) calculated at a scaled intensity of 2.5 times the experimental intensity. The black and green numbers in each panel indicate the measured and scaled intensity in units of 10^{14} W cm^{-2} for the experiment and theory, respectively.

energy $E_{\rm exc} = 13.5$ eV. After the inelastic recollision, the recolliding electron is propagated from the origin with an initial momentum $p = \sqrt{2(E_r - E_{\rm exc})}\cos\beta$, where β denotes the angle between the electron momentum just before and just after the recollision. The scattering angle β, the only free parameter of the model, accounts for scattering off the polarization axis, which reduces the momentum of the first electron along that axis.

The depletion of the excited state via ionization is calculated over the relevant intensity range by solving the rate equation

$$
\begin{aligned}
N_0(t+dt) &= N_0(t) - w_{01}N_0(t)dt,\\
N_1(t+dt) &= N_1(t) + w_{01}N_0(t)dt,\\
N_1^*(t+dt) &= N_1^*(t) + w_r(t)dt - w_{12}^*(t)N_1^*(t)dt,\\
N_2(t+dt) &= N_2(t) + w_{12}^*(t)N_1(t)dt,\\
N_{1,2}(t_i) &= 0, \quad N_1^*(t_i) = 0, \quad N_0(t_i) = 1,
\end{aligned}
$$

where $N_1^*(t)$ is the population of the excited state Ar^{+*} and $w_r(t)$ is the recollision excitation rate. To calculate the rate w_{12}^*, Eq. (A1) is used with the parameters $\alpha = 8$ and $I_p = 14.1$ eV.

All calculation results are intensity averaged over the focal volume assuming a Gaussian intensity profile in the interaction region and neglecting the intensity variation along the laser propagation axis. The limits of this approximation and their effect are discussed below.

APPENDIX B: PROCEDURE FOR FITTING THE MODEL CALCULATIONS TO THE MEASURED DATA

For the comparison of the experimental data with the semiclassical model, we follow the procedure used previously in Refs. [24,26] and determine the intensity, the pulse duration, and the absolute CEP from the CEP-dependent Ar^+ momentum spectrum recorded at the intensity $I = 1.2 \times 10^{14}$ W cm^{-2}. First, we use the CEP-averaged Ar^+ momentum spectrum to determine the intensity $I_{\rm th}$ that yields best agreement between the widths of calculated and measured spectra and find $I_{\rm th} = 3.0 \times 10^{14}$ W cm^{-2}, in agreement with the results of Ref. [24]. Second, the measured amplitude of the CEP-dependent Ar^+ asymmetry is used as a sensitive parameter for determination of the pulse duration. Best agreement with the experimental data, shown in Fig. 4, is

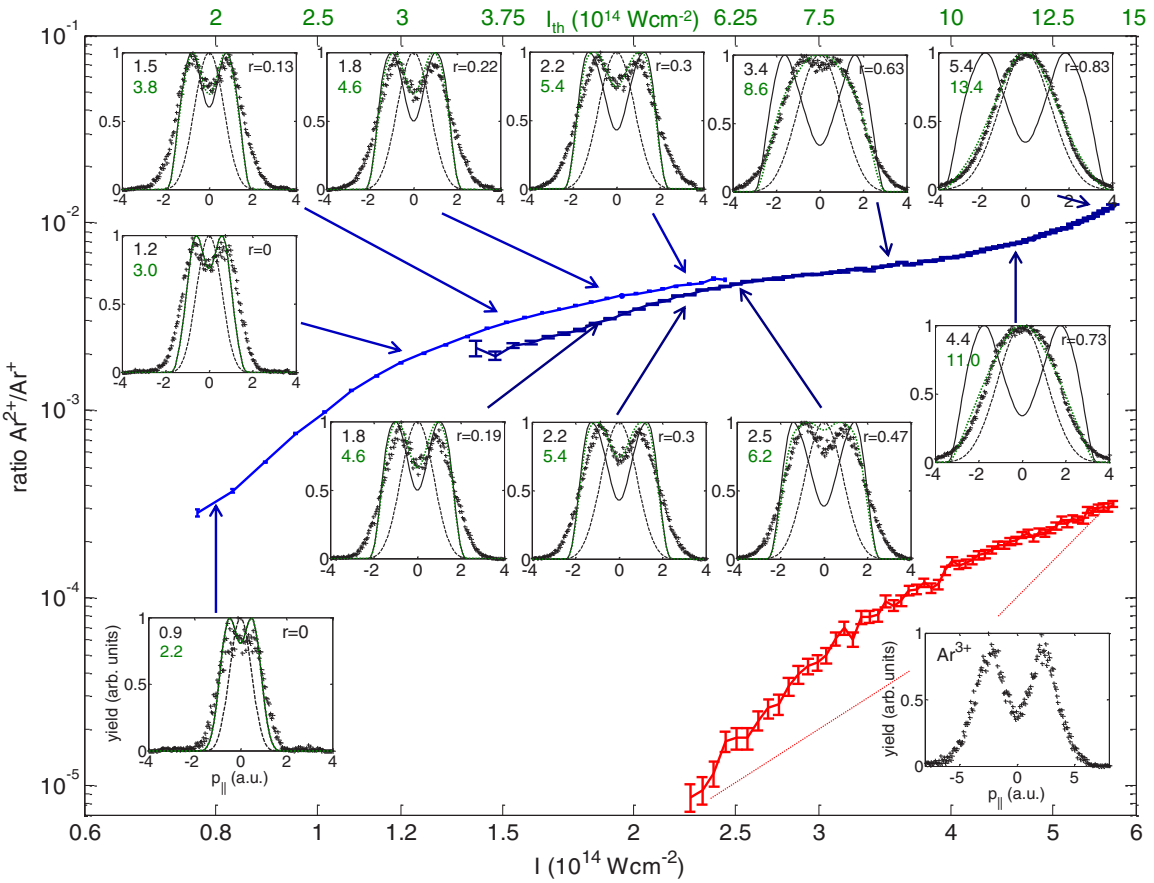

FIG. 6. Same as Fig. 1 but showing the CEP-averaged Ar^{2+} ion momentum spectra along the laser polarization instead of the TEMS. The measured spectra (black symbols) are shown together with the calculated ion momentum spectra assuming a weighted sum (solid green line) of RESD (solid line) and SDI (dashed line) contributions. The ratio r of SDI to the total signal is indicated in each panel. The lower intensity I axis denotes the measured intensity and the upper intensity axis $I_{\rm th}$ denotes the scaled intensity used in the calculations. The black and green numbers in each panel indicate, in units of 10^{14} W cm^{-2}, the measured and scaled intensities, respectively. All spectra are normalized to a peak value of 1. The red curve displays the yield ratio of Ar^{3+} to Ar^+. Also shown is the corresponding CEP- and intensity-averaged Ar^{3+} ion momentum spectrum.

obtained for a pulse duration of 4.0 fs (FWHM of the intensity envelope). Finally, the global offset value of the measurement CEP is determined by matching the phase of the measured Ar^+ asymmetry to the calculated one.

A particular asset of the experiment is that the laser intensity is varied by changing the laser power only. While the accuracy of the absolute intensity value is limited, the changes of the intensity are precisely proportional to the changes of the laser power. Because of this strict proportionality, all the other laser intensity values are entirely determined by the above procedure performed at a single intensity. The widths of the measured Ar^+ momentum spectra shown in Fig. 5 are reasonably well reproduced by the simulations performed at 2.5 times the experimental intensity.

Having used only one CEP-dependent Ar^+ spectrum at a single intensity value to infer all laser parameters, the only remaining free parameter is the scattering angle β, which is chosen to best fit the CEP-averaged TEMSs shown in Fig. 1. Following this systematic procedure ensures a fair comparison of theoretical results with the experimental data.

APPENDIX C: ION MOMENTUM SPECTRA

In Fig. 6, the measured ratio of double- to single-ionization yields is shown together with the corresponding CEP-averaged Ar^{2+} ion momentum spectra, along the laser polarization direction. The spectra reflect the corresponding intensity-dependent variations of the TEMSs discussed in the main text. With increasing intensity, the double-peak structure, characteristic of the NSDI regime, is progressively replaced by the growing contribution of the single-peak structure arising from SDI. This is similar to experimental results obtained using longer pulses [35,36]. This evolution of the Ar^{2+} spectra with intensity is qualitatively reproduced by the weighted sum (dotted green line) of the RESD (solid black line) and SDI (dashed black line) calculations, when the peak intensity I_{th} is used.

In addition to the data on double ionization, we present in Fig. 6 the ratio of triple- to single-ionization yields (red line) together with the corresponding CEP- and intensity-averaged Ar^{3+} momentum distribution, recorded in the high-intensity measurement. The pronounced double-peak structure of the Ar^{3+} momentum distribution is consistent with the results of previous studies by Rudenko *et al.* [5], who reported Ar^{n+} ($n = 2,3,4$) momentum distributions generated in few-cycle pulses. We would like to note, however, that the Ar^{3+} data are presented only for the sake of completeness, as a thorough discussion of these results is beyond the scope of the present paper.

APPENDIX D: SIMULATION OF THE ASYMMETRY USING THE MEASURED INTENSITY VALUES

It is interesting to note that when the calculations are performed with the measured intensity instead of the scaled one, much better agreement with the measurement is obtained for the asymmetry phases, as shown in Fig. 7(b). However, the asymmetry amplitudes shown in Fig. 7(a) is largely overestimated and it is clear from Figs. 6, 1, and 2 that in this case, none of the spectra are even qualitatively reproduced.

The different intensities needed to fit different observables can be explained as follows: While for the calculation of the momentum distributions and asymmetry amplitude the underestimation of momenta, inherent to the classical propagation, is artificially compensated by overestimating the intensity, the yield ratio and the phase of the CEP-dependent asymmetry are mostly independent of the momentum values. These quantities are thus not expected to be affected by the underestimation of momenta in the semiclassical model. That these quantities are better described with the measured intensity suggests that the single- and double-ionization rates used in the model are rather appropriate. Overcoming the shortcomings of the classical

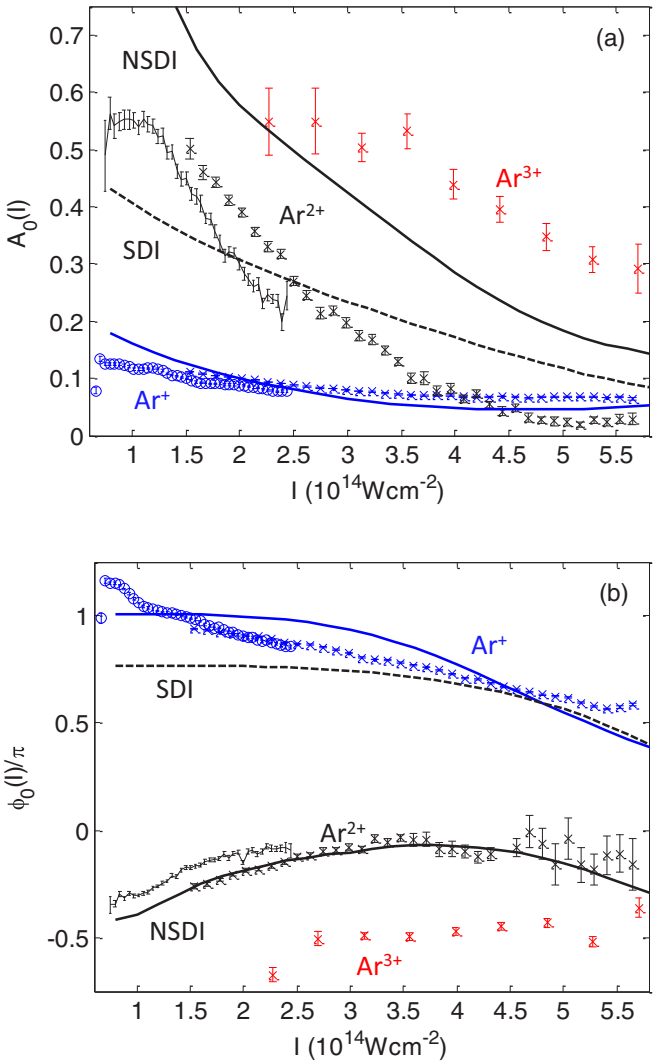

FIG. 7. Intensity dependence of the CEP-dependent asymmetries in the Ar^{n+} ($n = 1,2,3$) ion yields, encoded as blue, black, and red, respectively. The intensity dependences of $A_0(I)$ and $\phi_0(I)$ are shown in (a) and (b), respectively. The data recorded in the low-intensity and high-intensity measurements are represented by circles and crosses, respectively. The blue solid line corresponds to the SI calculations. The solid and dashed black lines display the predictions for Ar^{2+} by the semiclassical NSDI and SDI models, respectively. Here the unknown phase offset is chosen such that the values of $\phi_0(I)$ recorded for Ar^+ at $I = 1.5 \times 10^{14}$ W cm^{-2} agree with the result of the SI calculation. Here the calculations are performed using the measured intensity values and a laser pulse duration of 4.5 fs.

propagation will probably require a full quantum mechanical treatment, such as the one developed in Refs. [37,38].

APPENDIX E: DISCREPANCY BETWEEN THE HIGH- AND LOW-INTENSITY DATA SETS

Let us consider more closely the measured region in which the peak intensities of the high- and low-intensity data sets overlap. Due to the different focal lengths used in the two measurements, keeping a constant count rate of 0.1 counts per shot implies different geometries of the interaction region. While for a given intensity in the overlap region, the extension of the interaction region compared to the Rayleigh range is large for the high-intensity data set, it is small for the low-intensity data set. Thus, low intensities have a higher weight in the focal volume in the high-intensity data set, which results in the observed suppression of the yield ratio in that data set.

In order to quantify this effect, we fit the intensity-dependent yield ratio recorded in the low-intensity measurement with our model. For the purpose of the present discussion, we use a scaling intensity $I_{\mathrm{th}} = 1.55I$ to obtain the best fit with the measured data when the intensity variation along the laser propagation axis is neglected. The calculation results (blue lines) are plotted together with the measured data in Fig. 8. The red curves in Fig. 8 show the result of the same calculation, except that focal intensity averaging is performed over all three dimensions, i.e., accounting also for the intensity variation along the laser propagation axis. As can be seen in Fig. 8, the different focal geometries provide a quantitative explanation for the mismatch of the two yield ratio curves. The effect is further confirmed by applying the same procedure to the asymmetry curves of Fig. 3(a), since in that case, as well, the different focal geometries quantitatively explain the difference of the Ar^{2+} asymmetry between the two data sets.

The effect is also consistent with the similarities observed between the TEMS at 1.9×10^{14} W cm^{-2} in the first data set and 2.2×10^{14} W cm^{-2} in the second data set (see Fig. 1)

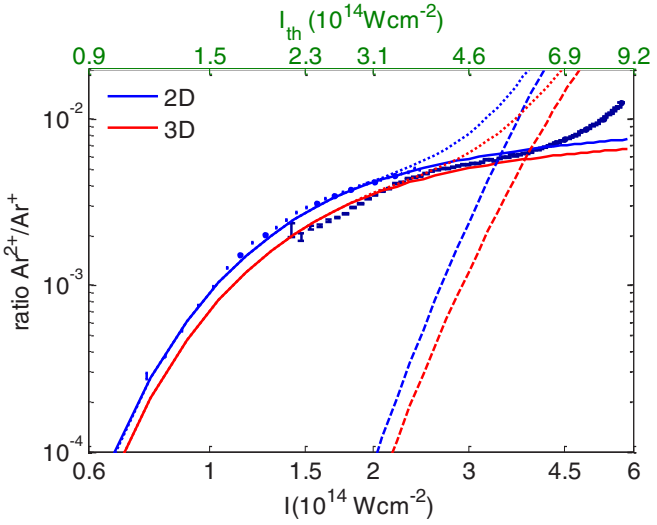

FIG. 8. The Ar^{2+} to Ar^{+} yield ratio measured in the low- and high-intensity measurements (light blue and dark blue symbols, respectively) is shown together with the calculated one, assuming NSDI (solid line) and SDI (dashed line). The sum of the contribution of both mechanisms is represented by the dotted line. A scaled intensity $I_{\mathrm{th}} = 1.55I$ and an excitation probability of 1% were used for the calculations. The calculated double-ionization yields were averaged over the focal volume assuming a Gaussian intensity profile for the two limiting cases of a 3D integration (red lines) and a 2D integration (blue lines) over the focal volume.

and the corresponding Ar^{2+} recoil momentum spectra shown in Fig. 6. The quantitative comparison of the two data sets provides a good example for the typical reproducibility of strong-field experiments performed under similar although not identical conditions. It further demonstrates how easily measured quantities can be fitted individually, merely by adjusting the intensity.

[1] B. Walker, B. Sheehy, L. F. DiMauro, P. Agostini, K. J. Schafer, and K. C. Kulander, Phys. Rev. Lett. **73**, 1227 (1994).

[2] S. Larochelle, A. Telebpour, and S. L. Chin, J. Phys. B **31**, 1201 (1998).

[3] R. Moshammer, B. Feuerstein, W. Schmitt, A. Dorn, C. D. Schröter, J. Ullrich, H. Rottke, C. Trump, M. Wittmann, G. Korn, K. Hoffmann, and W. Sandner, Phys. Rev. Lett. **84**, 447 (2000).

[4] T. Weber, H. Giessen, M. Weckenbrock, G. Urbasch, A. Staudte, L. Spielberger, O. Jagutzki, V. Mergel, M. Vollmer, and R. Dörner, Nature (London) **405**, 658 (2000).

[5] A. Rudenko, K. Zrost, B. Feuerstein, V. L. B. de Jesus, C. D. Schröter, R. Moshammer, and J. Ullrich, Phys. Rev. Lett. **93**, 253001 (2004).

[6] A. N. Pfeiffer, C. Cirelli, M. Smolarski, R. Dörner, and U. Keller, Nat. Phys. **7**, 428 (2011).

[7] P. Lambropoulos, Phys. Rev. Lett. **55**, 2141 (1985).

[8] R. Kopold, W. Becker, H. Rottke, and W. Sandner, Phys. Rev. Lett. **85**, 3781 (2000).

[9] P. J. Ho, R. Panfili, S. L. Haan, and J. H. Eberly, Phys. Rev. Lett. **94**, 093002 (2005).

[10] S. Palaniyappan, A. DiChiara, E. Chowdhury, A. Falkowski, G. Ongadi, E. L. Huskins, and B. C. Walker, Phys. Rev. Lett. **94**, 243003 (2005).

[11] Y. Zhou, C. Huang, Q. Liao, and P. Lu, Phys. Rev. Lett. **109**, 053004 (2012).

[12] A. l'Huillier, L. A. Lompre, G. Mainfray, and C. Manus, Phys. Rev. A **27**, 2503 (1983).

[13] W. Becker, X. Liu, P. J. Ho, and J. H. Eberly, Rev. Mod. Phys. **84**, 1011 (2012).

[14] R. Dörner, T. Weber, M. Weckenbrock, A. Staudte, M. Hattass, H. Schmidt-Böcking, R. Moshammer, and J. Ullrich, Adv. At. Mol. Opt. Phys. **48**, 1 (2002).

[15] J. Ullrich, R. Moshammer, A. Dorn, R. Dörner, L. P. H. Schmidt, and H. Schmidt-Böcking, Rep. Prog. Phys. **66**, 1463 (2003).

[16] M. Weckenbrock, D. Zeidler, A. Staudte, T. Weber, M. Schöffler, M. Meckel, S. Kammer, M. Smolarski, O. Jagutzki, V. R. Bhardwaj, D. M. Rayner, D. M. Villeneuve, P. B. Corkum, and R. Dörner, Phys. Rev. Lett. **92**, 213002 (2004).

[17] E. Eremina, X. Liu, H. Rottke, W. Sandner, M. G. Schätzel, A. Dreischuh, G. G. Paulus, H. Walther, R. Moshammer, and J. Ullrich, Phys. Rev. Lett. **92**, 173001 (2004).

[18] A. Rudenko, V. L. B. de Jesus, T. Ergler, K. Zrost, B. Feuerstein, C. D. Schröter, R. Moshammer, and J. Ullrich, Phys. Rev. Lett. **99**, 263003 (2007).
[19] A. Staudte, C. Ruiz, M. Schöffler, S. Schössler, D. Zeidler, T. Weber, M. Meckel, D. M. Villeneuve, P. B. Corkum, A. Becker, and R. Dörner, Phys. Rev. Lett. **99**, 263002 (2007).
[20] P. B. Corkum, Phys. Rev. Lett. **71**, 1994 (1993).
[21] Y. Liu, S. Tschuch, A. Rudenko, M. Dürr, M. Siegel, U. Morgner, R. Moshammer, and J. Ullrich, Phys. Rev. Lett. **101**, 053001 (2008).
[22] M. Kübel, K. J. Betsch, N. G. Kling, A. S. Alnaser, J. Schmidt, U. Kleineberg, Y. Deng, I. Ben-Itzhak, G. G. Paulus, T. Pfeifer, J. Ullrich, R. Moshammer, M. F. Kling, and B. Bergues, New J. Phys. **16**, 033008 (2014).
[23] N. Camus, B. Fischer, M. Kremer, V. Sharma, A. Rudenko, B. Bergues, M. Kübel, N. G. Johnson, M. F. Kling, T. Pfeifer, J. Ullrich, and R. Moshammer, Phys. Rev. Lett. **108**, 073003 (2012).
[24] B. Bergues, M. Kübel, N. G. Johnson, B. Fischer, N. Camus, K. J. Betsch, O. Herrwerth, A. Senftleben, A. M. Sayler, T. Rathje, T. Pfeifer, I. Ben-Itzhak, R. R. Jones, G. G. Paulus, F. Krausz, R. Moshammer, J. Ullrich, and M. F. Kling, Nat. Commun. **3**, 813 (2012).
[25] N. G. Johnson, O. Herrwerth, A. Wirth, S. De, I. Ben-Itzhak, M. Lezius, B. Bergues, M. F. Kling, A. Senftleben, C. D. Schröter, R. Moshammer, J. Ullrich, K. J. Betsch, R. R. Jones, A. M. Sayler, T. Rathje, K. Rühle, W. Müller, and G. G. Paulus, Phys. Rev. A **83**, 013412 (2011).
[26] B. Bergues, M. Kübel, N. G. Kling, C. Burger, and M. F. Kling, J. Sel. Top. Quantum Electron. **21**, 8701009 (2015).
[27] Y. Chen, Y. Zhou, Y. Li, M. Li, P. Lan, and P. Lu, J. Chem. Phys. **144**, 024304 (2016).
[28] A. S. Maxwell and C. Figueira de Morisson Faria, Phys. Rev. Lett. **116**, 143001 (2016).
[29] B. Feuerstein, R. Moshammer, D. Fischer, A. Dorn, C. D. Schröter, J. Deipenwisch, J. R. Crespo Lopez-Urrutia, C. Höhr, P. Neumayer, J. Ullrich, H. Rottke, C. Trump, M. Wittmann, G. Korn, and W. Sandner, Phys. Rev. Lett. **87**, 043003 (2001).
[30] C. F. de Morisson Faria, T. Shaaran, and M. T. Nygren, Phys. Rev. A **86**, 053405 (2012).
[31] F. Lücking, A. Assion, A. Apolonski, F. Krausz, and G. Steinmeyer, Opt. Lett. **37**, 2076 (2012).
[32] M. G. Pullen, W. C. Wallace, D. E. Laban, A. J. Palmer, G. F. Hanne, A. N. Grum-Grzhimailo, K. Bartschat, I. Ivanov, A. Kheifets, D. Wells, H. M. Quiney, X. M. Tong, I. V. Litvinyuk, R. T. Sang, and D. Kielpinski, Phys. Rev. A **87**, 053411 (2013).
[33] X. M. Tong and C. D. Lin, J. Phys. B **38**, 2593 (2005).
[34] M. V. Ammosov, N. B. Delone, and V. P. Krainov, Zh. Eksp. Teor. Fiz. **91**, 2008 (1986) [Sov. Phys. JETP **64**, 1191 (1986)].
[35] V. L. B. de Jesus, B. Feuerstein, K. Zrost, D. Fischer, A. Rudenko, F. Afaneh, C. D. Schröter, R. Moshammer, and J. Ullrich, J. Phys. B **37**, L161 (2004).
[36] A. Rudenko, T. Ergler, K. Zrost, B. Feuerstein, V. L. B. de Jesus, C. D. Schröter, R. Moshammer, and J. Ullrich, Phys. Rev. A **78**, 015403 (2008).
[37] C. F. de Morisson Faria and X. Liu, J. Mod. Opt. **58**, 1076 (2011).
[38] Z. Chen, Y. Liang, D. H. Madison, and C. D. Lin, Phys. Rev. A **84**, 023414 (2011).